JOURNAL OF PROPULSION AND POWER
Vol. 26, No. 2, March–April 2010

Improved Spray Model for Viscous Annular Sheets in a Swirl Injector

Yoonwan Moon,* Dongjun Kim,† and Youngbin Yoon‡
Seoul National University, Seoul 151-742, Republic of Korea

DOI: 10.2514/1.45010

A modified sheet breakup model was applied to a thin, viscous liquid film generated by a swirl injector similar to that installed in a liquid propellant rocket engine combustor. The sheet breakup model consists of three steps: determination of the swirl injector characteristics for the prediction of initial sheet conditions at the injector exit as input, linear stability analysis for primary sheet breakup, and the Taylor analogy breakup model for final drop formation. Under atmospheric pressure, the liquid sheet breakup occurs under a long-wave regime, sometimes according to simple theoretical analysis. But in high ambient pressure conditions, like a liquid propellant rocket engine combustor, the sheet breakup regime changes from a long wave to a short-wave regime due to a high gas Weber number ($We_2 > 27/16$), although the same injector was used. The sheet breakup model was, therefore, modified to be applicable to both long- and short-wave regimes and validated by the comparison of breakup length and Sauter mean diameter to experimental results. In both experimental and computational results, the spray cone angle and breakup length decreased as the ambient pressure increased, even though the pressure difference of the injector was constant. Local Sauter mean diameters, predicted by computation, were smaller at high ambient pressures. The comparative results show that the computational model is able to accurately predict sheet breakup length, spray cone angle, local Sauter mean diameter, and overall spray shape. Therefore, the model can be used as a design tool, ahead of analyzing spray characteristics of an injector in both atmospheric and high ambient pressure conditions.

Nomenclature

A	=	area
B	=	ratio of swirl arm to tangential entry radius
C_D	=	generalized equivalent discharge coefficient
D	=	droplet diameter
d	=	diameter
f	=	liquid mass fraction
h	=	(a half) thickness of sheet
i	=	number of tangential entry
K	=	geometrical characteristic constant
K_{eq}	=	generalized equivalent geometrical characteristic constant
K_s	=	most unstable wave number
k	=	wave number
L	=	breakup length
L_K	=	length of vortex chamber[5]
N	=	parcel number
Oh	=	Ohnesorge number
P	=	pressure
Q	=	density ratio ($=\rho_2/\rho_1$)
Re	=	Reynolds number
R_K	=	radius of vortex chamber
r_p	=	radius of tangential entry
r_r	=	radius of gas core at discharge nozzle
r'_r	=	radius of gas core at discharge nozzle exit
r_0	=	radius of discharge nozzle
S_B	=	dimensionless radius of gas core at the injector exit
t	=	time
U	=	sheet-gas relative velocity
V	=	absolute sheet velocity
We	=	Weber number
α	=	spray cone angle
ΔP	=	liquid injection pressure differential
Δ_K	=	energy loss due to friction in the swirling chamber
δV	=	grid cell volume
ε	=	jet deformation coefficient
η	=	wave amplitude
θ	=	friction factor
λ_k	=	friction coefficient
ν	=	coefficient of kinetic viscosity
ρ	=	density
σ	=	surface tension
τ	=	breakup time
Ω_s	=	maximum growth rate
ω	=	growth rate

Subscripts

amb	=	ambient
b	=	breakup
D	=	discharge or deformation
eq	=	equivalent
i	=	ith grid cell
in	=	inlet
liq	=	liquid
n	=	nth droplet
noz	=	contracting part of injector
sum	=	summation
0	=	initial or discharge nozzle exit
1	=	liquid phase
2	=	gas phase

Received 17 April 2009; revision received 9 October 2009; accepted for publication 4 November 2009.

*Ph.D. Candidate, School of Mechanical and Aerospace Engineering; Senior Researcher, Korea Aerospace Research Institute; ywmoon@kari.re.kr.

†Ph.D., School of Mechanical and Aerospace Engineering; Ministry of Education, Science, and Technology; kan31@snu.ac.kr.

‡Professor, Institute of Advanced Aerospace Technology, School of Mechanical and Aerospace Engineering, San 56-1, Shillim-dong, Gwanak-gu; ybyoon@snu.ac.kr.

I. Introduction

SWIRL injectors are widely used in industrial furnaces, agricultural sprays, automotive, gas turbine, and liquid propellant

rocket engines (LPREs). Advantages of swirl injectors include improved atomization, lower combustion instability, and wider operating range, due to their alteration of hydraulic spray characteristics [1,2]. In particular, a liquid–liquid coaxial swirl atomizer is known to efficiently generate high performance in LPREs (for example, the RD-107, RD-108, and RD-0110 engines installed in the booster, main core, and upper stage of Soyuz launch vehicles, respectively [3–5]).

A pressure-swirl atomizer generates a thin liquid sheet, spreading radially by a circumferential flow, which can be generated by using a screw or tangential entries in a vortex chamber. As the circumferential flow approaches the discharge orifice, it is accelerated by the converging part between the vortex chamber and the discharge orifice. Because of high tangential flow velocity, a gas core is formed around the injector centerline to balance the static pressure of the working fluid with the ambient pressure. At the injector exit, the liquid sheet is injected at a specific tangential angle corresponding to the ratio of the axial and tangential velocities. As the liquid sheet travels downstream from the injector exit, it becomes thinner and more unstable due to the amplification of the surface wave disturbance. When this disturbance reaches the most unstable state, fragmentation occurs abruptly. Fragmentation of the injected liquid into smaller fluid elements and their subsequent mixing and evaporation are of critical importance to combustion. The characteristics of the resulting spray field have a significant impact on the combustion stability as well as on the propulsion efficiency.

It is important to accurately predict initial sheet thickness, spray angle, and injection velocity, because those parameters are related to spray characteristics like downstream Sauter mean diameter (SMD) and spray distribution width. As an experimental study, Rizk and Lefebvre [6] showed a correlation between sheet thickness at the injector nozzle exit and downstream SMD for an air-blast atomizer with coflow. Bayvel and Orzechowski [1] and Lefebvre [2] theoretically derived a relation between spray characteristics and injector geometry from steady inviscid hydrodynamic analysis. However, inviscid hydrodynamic analysis over/underestimates the initial spray characteristics, due to the absence of friction losses [7]. According to Zong and Yang [7], inviscid theory overpredicted the spray cone angles by almost 25% and underpredicted the film thickness by a maximum of 30%. Borodin et al. [8], Dityakin et al. [9], and Bazarov et al. [10] derived a general relation based on inviscid analysis that considered viscous effects. Inamura et al. [11] determined initial sheet thicknesses and spray angles of several conical sheets using the boundary layer theory and compared them to experimental results. Davy and Loustalan [12] determined sheet breakup length experimentally by a void fraction analysis and compared experimental results with predictions obtained by three breakup models. They suggested that the prediction of breakup length was very sensitive to the velocity coefficients used in the various breakup models.

Macroscopic theoretical research has been performed to investigate the spray characteristics of a pressure-swirl atomizer, and the fragmentation phenomena of liquid sheets was theoretically and experimentally examined to understand breakup mechanisms [13]. Dombrowski and Johns [14] have speculated that drop sizes may be related to the wavelengths that grow on the sheet surface. They derived a dispersion relation for the growth rates of long waves with infinitesimal amplitude, which included the effects of surface tension, aerodynamic forces, and liquid viscosity. Their analysis identified the wavelength with the largest growth rate, assuming that the wave broke up the sheet at half-wavelength intervals into ligaments. Such ligaments are broken up into droplets, according to Weber's theory for cylindrical liquid columns [14]. Stapper et al. [15] have reported the existence of two sheet breakup mechanisms: a stretched streamwise ligament breakup regime occurring at low liquid velocities associated with coflowing air and a cellular breakup regime occurring at higher relative liquid velocities. In the latter regime, both streamwise and spanwise waves exist, and the spanwise waves caused the sheet to break into ligaments. This spanwise wave breakup process is similar to that suggested by Dombrowski and Johns [14] and Senecal et al. [13].

Early researchers assumed the fluid was inviscid. Dombrowski and Johns [14] used a one-dimensional liquid film model, based on inviscid theory simplified by long-wave assumptions. Dombrowski and Hassan [16] and Jones [17] have emphasized that, for low-viscosity liquids, simple inviscid analysis provides a basic understanding of the flow characteristics of pressure-swirl atomizers and gives a reasonable guide to discharge coefficients and cone angles. Han et al. [18] and Ren and Nally [19] applied this model to a hollow-cone spray. Binnie and Harris [20] showed that, although the motion in the bulk of the fluid can be considered irrotational, the viscous effect of the retarded boundary layer cannot be regarded as negligible. Moreover, long-wave assumption leads to inaccurate predictions on the sheet stability of modern atomizers under the conditions of high injection pressure and high ambient pressure [13].

A linear stability analysis is very useful to understanding the breakup phenomena of liquid columns or sheets. Sterling and Sleicher [21] and Reitz and Bracco [22] conducted analyses of cylindrical liquid jets, and Senecal et al. [13] derived a liquid sheet breakup formulation for a swirl atomizer using linear stability theory, including the viscosity effects between the surrounding gas and liquid. Their model can be readily implemented in multidimensional simulations of transient sprays. Li and Tankin [23] developed a general dispersion relation, including the effects of viscosity. However, it is somewhat cumbersome to use in multidimensional models, because their viscous-based results required the numerical solution of a complex nonlinear equation. The most commonly used analysis for the onset of liquid jet atomization is based on the linear theory, which only considers a disturbance growing with time (temporal linear theory). However, Lin [24] recently developed a linear theory considering a disturbance evolving in space and time (spatiotemporal linear theory). This new linear theory predicted convective instability well, which is incorrectly predicted by temporal linear theory. Therefore, he insisted that it was necessary to consider spatial disturbances as well as temporal disturbances.

Linear stability analysis is already known: it was implemented by many researchers as mentioned previously, but the applications of linear stability analysis by computational fluid dynamics were mainly used to analyze the spray characteristics of diesel engines or gasoline direct ignition engines [13,18,19]. These injectors, installed in automotive engines, generate wavy sheets with short-wave regimes because of high injection velocity (a few hundred meters per second) due to the pressure difference of the injector. On the other hand, swirl injectors installed in LPREs with a gas generator cycle usually have a small injection pressure difference ($10 \sim 15$ bar) and a small injection velocity (several tens of meters per second); long-wave regimes, as well as short-wave regimes, may be found in accordance with test conditions. To predict the spray characteristics in a noncombusting environment (e.g., hydraulic injector test), both regimes should be considered. Therefore, this study focused on the extension of the application of the linear stability analysis, although many researchers have studied and applied it. Also emphasized in this study was the accurate prediction of initial characteristics of wavy sheets (film thickness and spray-cone-angle-considering friction losses, etc.) as input by using injector design procedure and viscous theory [8–10]. These considerations are commonly used when simplex swirl injectors are designed with databases constructed by Russian rocketry. The accurate prediction of inlet characteristics of wavy sheets is especially important in affecting the characteristics of the spray disintegrated from a wavy sheet. When LPRE combustor is designed, several injectors are considered in the preliminary design phase. Because all of the designed injectors cannot be tested, an injector designer should choose two or three injectors, having good performance, by analyzing the spray characteristics of the injectors: this is the aim of developing this model. There are two aims of the present study: extending the application of the linear stability analysis from automotive engines to LPRE and accurately predicting the inlet conditions of the spray field by using common injector design theory, considering energy losses due to viscosity.

In the present study, to investigate the spray characteristics of a swirl injector, a modified sheet breakup model was applied to a thin

viscous liquid film generated by a swirl injector installed in a liquid propellant rocket engine combustor. For accurate prediction of initial film thickness, spray cone angle, and injection velocity, a viscous theory for the swirl injector design procedure by Borodin et al. [8], Dityakin et al. [9], and Bazarov et al. [10] is adopted. Also, the simplified linear stability analysis suggested by Senecal et al. [13] is adopted to model the dispersion of the spray after being injected. To validate the usefulness of the sheet breakup model from low to high gas Weber numbers, defined as the liquid Weber number multiplied by the density ratio of gas to liquid, the computations in various ambient pressures were performed. First, the spray characteristics in atmospheric condition (such as the breakup length, spray cone angle, and the SMD) were computed for various pressure differences of the injector and compared with the experimental results for validation. Second, based on the model validation in the atmospheric condition, the computations at various ambient pressures were performed at a fixed pressure drop of the injector and compared with the experimental results with respect to breakup length and spray cone angle. Also, the SMD was predicted by this model.

II. Numerical Approaches

A. Prediction Methodology for Initial Spray Characteristics

In the KIVA (internal combustion engine simulation code) program, the initial spray characteristics are treated as input by an external file [25]. Therefore, the initial spray characteristics (such as input) should be based on experimental data. But it is difficult to predict those characteristics as input if there are no experimental data for new injectors. That is cumbersome for injector designers. In the present study, to eliminate the cumbersome calculations, the geometrical information, the mass flow rate, and the target pressure difference of the injector are needed. The procedure for calculating the initial spray characteristics was implemented inside the KIVA program to predict more accurate inlet conditions at the injector exit.

1. Definition of Main Parameters of Swirl Injector Using Inviscid Theory

A simplex atomizer model is presented in Fig. 1 and consists of several parts: the length of the vortex chamber L_k, the radius of the vortex chamber r_k, the radius of the tangential inlet r_p, the radial location of the tangential entry $R = r_k - r_p$, the radius of the orifice r_0, the radius of the gas core in the orifice r_r, and the radius of the gas core at the orifice exit r_r'. In the region of the swirl chamber, the motion consists of a potential vortex caused by a negative source for which the position coincides with the apex of the transient cone at the cylindrical discharge orifice exit. In the cylindrical discharge orifice region, there is a potential vortex along with an axial motion. All velocities (i.e., axial u, circumferential v, and radial w) should be considered, but radial velocity w is negligible because it is significantly lower than the others. The geometric constant K, which determines the swirling strength of the injected fluid, is defined as $K \equiv A_0 R/A_{\text{in}} r_0$, with the orifice area A_0 and the total area of the tangential inlets A_{in}. According to the conservation laws of energy and the angular momentum for an inviscid flow in a maximum flow principle, injector geometric constant K can be expressed as [1,8–10]

$$K = \frac{(1-\varphi)\sqrt{2}}{\varphi\sqrt{\varphi}} \tag{1}$$

where the coefficient of passage fullness φ is defined as [1,8–10]

$$\varphi = 1 - \left(\frac{r_r}{r_0}\right)^2 \tag{2}$$

The spray cone angle is determined by the ratio of the tangential to the axial velocities at the injector exit. Applications of the Bernoulli equation and the law of angular momentum conservation for an inviscid flow show that spray cone angle is a function of a discharge coefficient C_D, a geometric constant K, and a dimensionless vortex radius at the injector exit $S_B(=r_r'/r_0)$, as determined by [1,8–10]:

$$\tan\frac{\alpha}{2} = \frac{2C_D K}{\sqrt{(1+S_B)^2 - 4C_D^2 K^2}} \tag{3}$$

Film thickness h_0 is defined by the coefficient of passage fullness φ as [1,8–10]

$$h_0 = r_0 - r_r = r_0(1 - \sqrt{1-\varphi}) \tag{4}$$

Liquid jets flowing through tangential entries impinge with the liquid rotating inside the swirl chamber. As a result, the liquid jets contract. There is a simultaneous increase of swirl radius, as shown in Fig. 1b, which leads to a decreased discharge coefficient C_D [1,8,9]. If liquid jet deformation is considered, the geometric constant should become [8,9]

$$K_D = \frac{K}{\varepsilon} \tag{5}$$

The jet deformation coefficient ε is the ratio of the swirl radius at the tangential entry to the swirl radius in the swirling chamber. Dityakin et al. [9] found that ε was a function of the parameter $B = R/r_0$. In this study, ε was obtained by fitting to the Dityakin et al. curve (Fig. 2) [9].

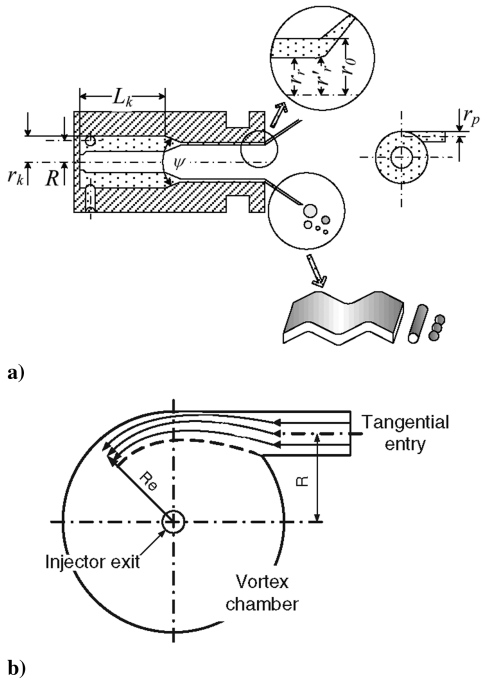

Fig. 1 Simplex atomizer mode: a) processes of sheet disintegration and b) schematic of liquid sheet deformation.

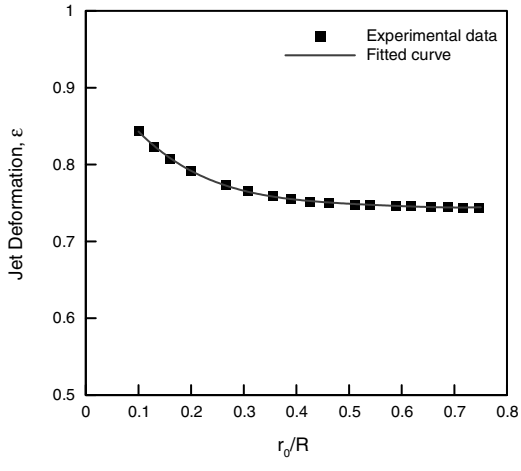

Fig. 2 Coefficient of inlet jet deformation ε according to $r_0/R(=1/B)$.

Equations (1–4) are basic parameters to design and determine characteristics of a swirl injector. The definitions and forms of each parameter will not change, even when liquid viscosity is considered.

2. Viscous Liquid Theory and Energy Loss

Friction coefficients and hydraulic parameters of injectors can be affected by liquid viscosity. The higher the viscosity, the higher the discharge coefficient and the lower the spray angle. To calculate an exact discharge coefficient, a friction coefficient due to viscosity in the swirling chamber should be considered. Dityakin et al. [9] obtained a friction coefficient, which depends on the Reynolds number of a tangential entry, as a result of tests with water and water/glycerin mixtures, with geometric constants varying from K_D 1.5 to 9.0. Water was used in the current study, and the friction coefficient λ_k was determined by [9]

$$\lambda_k = \begin{cases} \frac{24.6}{Re_{\text{in}}^{0.75}}, & (Re_{\text{in}} \le 2.3 \times 10^3) \\ \frac{1.22}{Re_{\text{in}}^{0.36}}, & (Re_{\text{in}} > 2.3 \times 10^3) \end{cases}; \qquad Re_{\text{in}} = \frac{V_{\text{in}} d}{\nu_1} \tag{6}$$

The tangential entry Reynolds number Re_{in} is defined by the inlet velocity V_{in}, and the equivalent inlet diameter is given by $d = \sqrt{i} d_p$. Because of swirling chamber friction, initial angular momentum decreases as flow approaches the orifice. Borodin et al. [8] and Bazarov et al. [10] implemented an angular momentum ratio to consider the friction between the tangential entry and the vortex chamber end by using angular momentum conservation. Therefore, the injector equivalent geometric constant K_{eq}, considering friction, should be expressed as

$$K_{\text{eq}} = \frac{K_D}{1+\theta} = \frac{(1-\varphi_c)\sqrt{2}}{\varphi_c \sqrt{\varphi_c}}; \qquad \theta = \frac{\lambda_k}{2} K_D \left(\frac{r_K}{r_0} - 1 \right) \tag{7}$$

Also, Borodin et al. [8] implemented energy loss caused by friction force acting on the vortex chamber end wall. The energy loss can be expressed as

$$\Delta E = \frac{\rho_1 Q^2}{2\pi^2 r_c^4} \Delta_K \tag{8}$$

Considering energy loss [Eq. (8)], the discharge coefficient can be expressed as [8]

$$C_D = \frac{1}{\sqrt{[K_{\text{eq}}^2/(1-\varphi_c)] + (1/\varphi_c^2) + \Delta_K}} \tag{9}$$

where

$$\Delta_K = \frac{\lambda_K}{\sigma^2} \left\{ \frac{1}{\sigma} \left(1 - \frac{1}{C_K} \right) + \lambda_K \left[\left(\frac{K_D}{2} - \frac{1}{2\sigma - \lambda_K} \right) \times \left(\frac{2}{\sigma} + \frac{K_D}{2} + \frac{1}{2\sigma - \lambda_K} \right) + \frac{3}{2\sigma^2} \ell_n \frac{(2\sigma - \lambda_K) K_D C_K}{2} \right] \right\}$$

$$\sigma = \frac{1}{K_D} + \frac{\lambda_K}{2} C_K; \qquad C_K = \frac{r_K}{r_0} \tag{10}$$

Hydraulic loss related to the swirling chamber length should be considered if the length is long. It was implemented by angular momentum conservation [9]. Hydraulic loss related to the swirling chamber length was determined as

$$\Delta_L = \frac{K_D^2}{2C_K} (1 + \mu_{pr} K_D C_K) \left[1 - \frac{1}{(1 + \theta [C_K/(C_K - 1)] \bar{\lambda} \cdot \bar{L}_K)^2} \right]$$

$$\bar{\lambda} = 1.0; \qquad \bar{L}_K = \frac{L_K}{D_K} \tag{11}$$

Here, μ_{pr} is a function of K_{pr}, defined as $K_{pr} = K_D \cdot C_K$. Further, K_{pr} is represented as

$$K_{pr} = (1 - \varphi_{pr}) \cdot 2^{0.5} / \varphi_{pr}^{1.5}$$

Therefore, μ_{pr} can be obtained from

$$\mu_{pr} = [\varphi_{pr}^3 / (2 - \varphi_{pr})]^{0.5}$$

where $\bar{\lambda}$ is the ratio of friction coefficient at the vortex chamber side wall to the vortex chamber end wall. According to Dityakin et al. [9], the consideration of loss, in accordance with the length of the vortex chamber, affects the discharge coefficient seriously if the friction factor θ is over approximately 0.25 [Eq. (7)]. When this loss was not considered, the discharge coefficient was overpredicted by a maximum of 56% when compared with experimental results. But if the loss is considered, the deviation of the discharge coefficient between the calculated and the experimental results can be reduced to 18%. However, it overpredicts also: the reason is the assumption that $\bar{\lambda} = 1$. According to Dityakin et al. [9], this assumption was excessive. Because the friction coefficient at the vortex chamber side wall cannot be obtained, it is assumed that the coefficient at the vortex chamber side wall is equal to the friction coefficient at the vortex chamber end wall λ_k [9]. Obtaining the factors related to the friction coefficient according to vortex chamber length will be another research project.

3. Other Friction Losses

According to Borodin et al. [8], Dityakin et al. [9], and Bazarov et al. [10], there are several hydraulic losses in the injector, which can affect spray characteristics. These losses cannot be handled by viscous liquid theory, because they depend on the design of swirl injector. But in order to accurately predict film thickness, spray cone angle, injection velocity, and downstream SMD, energy losses related to the tangential entry (Δ_{in}) and the converging part (Δ_{noz}) should be considered [8–10]. Energy loss occurring at the tangential entry may be determined by

$$\Delta_{\text{in}} = \xi_{\text{in}} \frac{K_D^2}{C^2}; \qquad C = \frac{R}{r_0} \tag{12}$$

where ξ_{in} is an inlet resistance coefficient and a function of the Reynolds number in the tangential inlet. The inlet resistance coefficient is similar to the loss coefficient in a pipe flow from the viewpoint of definition [1]. Therefore, the inlet resistance coefficient should be obtained from experimental data. In the present study, the inlet resistance coefficient was obtained by averaging the experimental data from Borodin et al. [8].

Hydraulic loss in the converging part of the injector [8,9] was determined by

$$\Delta_{\text{noz}} = \frac{\xi_{\text{noz}}}{\varphi_\theta^2} \tag{13}$$

where ξ_{noz} is the hydraulic resistance related to the contraction part angle; $\xi_{\text{noz}} = 0.11$ at $\psi = 90$ deg and $\xi_{\text{noz}} = 0.16$ at $\psi = 120$ deg.

The typical angle of the converging part is from 90 to 120 deg, and the hydraulic resistance is almost linear in this range [8,9].

The major losses of energy by friction were considered. Therefore, a generalized equivalent geometric constant K_{eq}, considering energy losses, is

$$K_{\text{eq}} = \frac{K_D}{1 + \theta \{ 1 + [C_K/(C_K - 1)] \bar{\lambda} \bar{L}_K \}} = \frac{(1 - \phi_\theta)\sqrt{2}}{\phi_\theta \sqrt{\phi_\theta}} \tag{14}$$

The discharge coefficient $C_{D\text{eq}}$, corresponding to Eq. (14), is [8–10]

$$C_{D\text{eq}} = \frac{1}{\{(1/\varphi_\theta^2) + [K_{\text{eq}}^2/(1 + \varphi_\theta)] + \Delta_{\text{sum}}\}^{0.5}}$$

$$\Delta_{\text{sum}} = \Delta_K + \Delta_{\text{in}} + \Delta_{\text{noz}} + \Delta_L \tag{15}$$

where the total energy loss due to friction Δ_{sum} is the sum of the local frictional losses [Eq. (15)].

In real circumstances, the thin film produced by the swirl flow is distorted at the injector end due to centrifugal force (Fig. 1).

If centrifugal force is considered, film thickness at the injector exit should be acquired from S_B instead of φ_θ. S_B can be obtained by numerically solving Eq. (16) [8–10]:

$$C_{D\text{eq}} = (1 - C_{D\text{eq}}^2 K_{\text{eq}}^2) - S_B(S_B^2 - C_{D\text{eq}}^2 K_{\text{eq}}^2)^{0.5} - C_{D\text{eq}}^2 K_{\text{eq}}^2 \ln \frac{1 + (1 - C_{D\text{eq}}^2 K_{\text{eq}}^2)^{0.5}}{S_B + (S_B^2 - C_{D\text{eq}}^2 K_{\text{eq}}^2)^{0.5}} \tag{16}$$

Film thickness at the injector end can then be defined as

$$h_0 = r_0(1 - S_B) \tag{17}$$

The spray cone angle can be calculated by replacing C_D and K by $C_{D\text{eq}}$ and K_{eq}, respectively, in Eq. (3). However, the spray cone angle is difficult to predict accurately, because it is strongly related to the injector geometry and the definition of the spray cone angle in the atomized spray field. Through the viscous liquid theory, a trend of the spray cone angle will be predicted. According to Bayvel and Orzechowski [1], the discharge coefficient considered in Eq. (12) agreed well with the experimental results. But, as shown in Eq. (12), the length of the tangential entry was not considered in the energy loss. Also, Bayvel and Orzechowski [1] pointed out that the length of tangential entry affects the spray cone angle severely in some cases. It is indicated that the discharge coefficient is less sensitive than the spray cone angle. This shows the difficulty of finding the accurate spray cone angle by a simplified analysis. If the boundary layer theory is used, some losses will be considered, and a more accurate spray cone angle will be obtained, like Inamura et al. [11] and Zong [26]. But it is impossible to find every loss acting on the swirl injector. Hence, a spray cone angle acquired from the modified Eq. (3) should be corrected by Fig. 3 [21].

Injection velocity is important, because the maximum growth rate of a liquid wave is a function of injection velocity. Actual injection velocity is different from theoretical velocity because of friction losses [1], as well as geometrical characteristics and pressure differences [2]. The ratio of real to theoretical velocity is the velocity coefficient. According to Lefebvre [2], the velocity coefficient is related to the discharge coefficient, film thickness, and spray cone angle. However, Davy and Loustalan [12] pointed out that determining sheet velocity using a velocity coefficient could yield unexpected results, such as predicting breakup lengths shorter than experimental results. To exclude the potential effects of velocity coefficients, sheet velocity was calculated using the discharge coefficient, the film thickness, and the spray cone angle, including frictional losses [1]. Hence, film axial velocity is defined as [1,8–10]

$$u = \sqrt{1 - \frac{4C_{D\text{eq}}^2 K_{\text{eq}}^2}{(1 + S_B)^2}} \sqrt{\frac{2\Delta P}{\rho}} \tag{18}$$

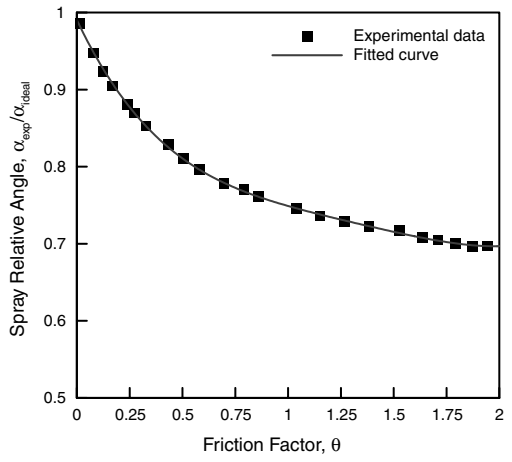

Fig. 3 Spray relative angles according to friction factor θ.

Injection velocity may be obtained by the definition

$$V = \frac{u}{\cos(\alpha/2)} \tag{19}$$

Because the liquid sheet has a tangential velocity due to swirl, the tangential velocity must be considered. As the injection velocity and the spray cone angle are known from Eqs. (18) and (19), the tangential velocity can be obtained easily as follows:

$$v = V \sin(\alpha/2) \tag{20}$$

B. Linear Stability Analysis

Senecal et al. [13] implemented dispersion relations between the growth rate ω and the wave number k for the cases of sinuous and varicose waves, respectively. Their dispersion relation for sinuous waves was

$$\omega^2[\tanh(kh) + Q] + \omega[4\nu_1 k^2 \tanh(kh) + 2iQkU] + 4\nu_1^2 k^2 \tanh(kh) - 4\nu_1^2 k^3 \mathcal{L} \tanh(\mathcal{L}h) - QU^2k^2 + \frac{\sigma k^3}{\rho_1} = 0 \tag{21}$$

Here, $\mathcal{L}^2 = k^2 + \omega/\nu_1$.

Based on the liquid sheet inviscid analysis of Senecal et al. [13], the maximum sinuous wave growth rate would always be greater or equal to the maximum varicose wave growth rate in the present study. Also, if the density ratio ($Q = \rho_2/\rho_1$) is near unity (e.g., $\rho_2 \geq 0.25\rho_1$), the varicose wave is less stable and plays an important role in the breakup of the liquid sheet [27]. However, in a LPRE combustor environment, Q has an order of magnitude between 10^{-3} and 10^{-2}. When Q is significantly less than one, it is assumed that sinuous waves dominate. In the present study, a sinuous wave for breakup is considered.

The Dombrowski and Johns [14] assumption on growth rate with long waves was acceptable for low gas Weber numbers $We_2 = \rho_2 U^2 h/\sigma$, but it was not appropriate for high gas Weber numbers. Therefore, a long or short-wave determination criterion was needed. Senecal et al. [13] suggested that the criterion We_2 was 27/16. In the present study, if $We_2 \leq 21/16$, the long-wave assumption is selected; if not, short waves are assumed. In general, a coaxial swirl injector installed in a LPRE combustor is operated by small injector pressure differences, because the LPRE system is restricted by turbo pump unit discharge pressure. In an atmospheric pressure environment, the long wave dominates the sheet characteristics generated by a swirl injector, due to low injection velocity and low gas phase density; however, the short wave dominates in a high-pressure environment, such as a LPRE combustor, because of high gas phase density, even when predicting sheet characteristics at both low and high ambient pressure. In the present study, both long and short-wave assumptions were applied.

The liquid sheet inviscid analysis presents guidelines for understanding sheet dispersion relations. However, to describe sheet prediction relations accurately, the effect of viscosity must be considered. In Eq. (21), the second-order viscosity terms can be ignored following an order-of-magnitude analysis using typical values of the most unstable wave number K_S and the maximum growth rate Ω_S from the inviscid solutions [13]. Thus, for the sinuous mode, the growth rate of the simplified Eq. (21) becomes

$$\omega_r = -\frac{2\nu_1 k^2 \tanh(kh)}{\tanh(kh) + Q} + \frac{\sqrt{4\nu_1^2 k^4 \tanh^2(kh) - Q^2U^2k^2 - [\tanh(kh) + Q](-QU^2k^2 + \sigma k^3/\rho_1)}}{\tanh(kh) + Q} \tag{22}$$

For long waves, two assumptions are applied to Eq. (22) [13]. The first assumption is that long waves grow on the interfaces, so that $\tanh(kh) \approx kh$, and the second is $Q \ll kh$. After applying these assumptions, Eq. (22) reduces to

$$\omega_r = -2\nu_1 k^2 + \sqrt{4\nu_1^2 k^4 + \frac{QU^2 k}{h} - \frac{\sigma k^2}{\rho_1 h}} \tag{23}$$

Furthermore, if short waves are assumed for high gas Weber number sheets and $Q \ll kh$, Eq. (22) reduces to [13]

$$\omega_r = -2\nu_1 k^2 + \sqrt{4\nu_1^2 k^4 + QU^2 k^2 - \frac{\sigma k^3}{\rho_1}} \tag{24}$$

C. Sheet Breakup and Drop Formation

To predict drop size by primary breakup, the sheet disintegration mechanism proposed by Dombrowski and Johns [14] is adopted. As shown in Eqs. (23) and (24), whereas long-wave growth rate depends on the sheet thickness, short-wave growth rate is independent of the sheet thickness. Therefore, in short waves, the onset of ligament formation can be predicted using a sheet breakup length formulated and based on an analogy of the prediction of the breakup length of the cylindrical liquid jets [22]. The breakup time τ and the length L are [13]

$$\tau = \frac{1}{\Omega_s}\ell_n\left(\frac{\eta_b}{\eta_0}\right) \tag{25}$$

$$L = V\tau = \frac{V}{\Omega_s}\ell_n\left(\frac{\eta_b}{\eta_0}\right) \tag{26}$$

The quantity $\ell_n(\eta_b/\eta_0)$ is given the value of 12, suggested by Dombrowski and Hooper [28].

For attenuating sheets, the long-wave sheet thickness is proportional to the radial distance from the injector nozzle and, thus, h in Eq. (23) changes with time [13]. Therefore, the growth rate must be integrated over time as [13]

$$\ell_n\left(\frac{\eta}{\eta_0}\right) = \int_0^t \omega \, \mathrm{d}t' \tag{27}$$

Senecal et al. [13] reported that the effect of viscosity was minimal for Squire's regime (i.e., for $We_2 < 27/16$; long-wave growth). Instead of Eq. (23) to predict the breakup length for the long-wave regime, the simplified growth rate can be calculated as

$$\omega_r = \sqrt{\frac{QU^2k^2 - \sigma k^3/\rho_1}{kh}} \tag{28}$$

Figure 4 shows that sheet thickness along the radial distance can be expressed geometrically. Hence, the local sheet length is $l = Vt$:

$$h = \frac{h_0(d_0 - h_0)}{d_0 - h_0 + 2Vt\sin(\alpha/2)} \tag{29}$$

By substituting Eq. (29) into Eq. (28) and integrating Eq. (27), the sheet breakup length $L = V\tau$ can be expressed as

$$L = \frac{1}{2\sin\frac{\alpha}{2}}\left[3V\sin\frac{\alpha}{2}\ell_n\left(\frac{\eta_b}{\eta_0}\right)\sqrt{\frac{h_0(d_0-h_0)}{QU^2k - \sigma k^2/\rho_1}} + (d_0 - h_0)^{3/2}\right]^{2/3} \tag{30}$$

The vertical breakup length z_b can be expressed as

$$z_b = L \times \cos\frac{\alpha}{2} \tag{31}$$

Ligaments are assumed to be formed at the breakup point as determined by either Eqs. (26) and (30), and their diameter can be obtained by mass balance. For short waves, ligaments are assumed to be formed from tears in the sheet, once per wavelength, and the resulting diameter is [13]

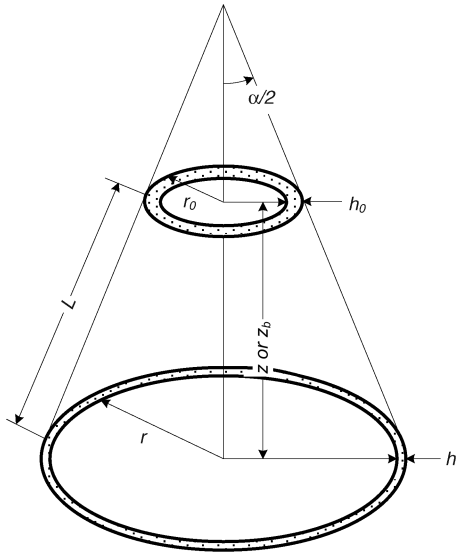

Fig. 4 Schematics of sheet thickness change in an annular liquid sheet.

$$d_L = \sqrt{\frac{16h}{K_S}} \tag{32}$$

where the most unstable wave number K_S is determined from Eq. (24). For long waves, it is assumed that the ligaments are formed from tears in the sheet, twice per wavelength, with the resulting diameter given by [13]

$$d_L = \sqrt{\frac{8h}{K_S}} \tag{33}$$

where the most unstable wave number K_S for long-wave growth is given by [13]

$$K_S = \frac{\rho_2 U^2}{2\sigma} \tag{34}$$

The primary breakup into drops occurs when the unstable wave amplitude is equal to the ligament radius, and that one drop will be formed per wavelength [14]. To calculate the most unstable wave number for a ligament, Weber's result for the breakup of a cylindrical, viscous liquid column was used [13]. Thus, the diameter of a drop that is broken from a ligament is

$$d_D = 1.88 d_L(1 + 3Oh)^{1/6} \tag{35}$$

where Oh is the Ohnesorge number and defined as $Oh = \mu_1/(\rho_1\sigma d_L)^{1/2}$.

III. Experimental and Numerical Setup

A. Experimental Setup

The experimental swirl injector (Fig. 5) was designed according to the hydraulics of Bayvel and Orzechowski [1]. The orifice diameter d_0 was 2 mm, and the tangential inlet had three 1-mm-diam holes d_p at 120 deg intervals. The injector was a closed type with a separate vortex chamber and orifice. The converging diameter ratio of the vortex chamber to the orifice was three. To investigate the effects of ambient gas pressure and injection velocity on spray characteristics, the high-pressure chamber system was used, as shown in Fig. 6.

Spray angle and breakup length were measured from instantaneous spray images taken by indirect photography. A stroboscopic light with an illuminating time of ≤ 4 μs was shone through translucent paper located behind the gas curtain (Fig. 6). The exposure time of a digital camera (Canon EOS 20D, 3504×2336) was identical to the flash interval of the stroboscope and set to take one image per flash without additional synchronization. The spray angle was the angle between the injection axis and the connecting

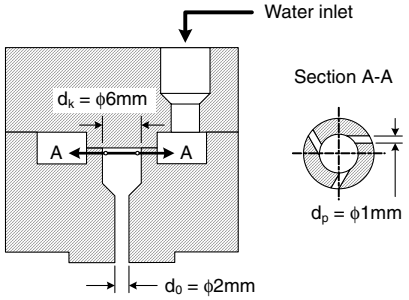

Fig. 5 Schematics of coaxial swirl injector.

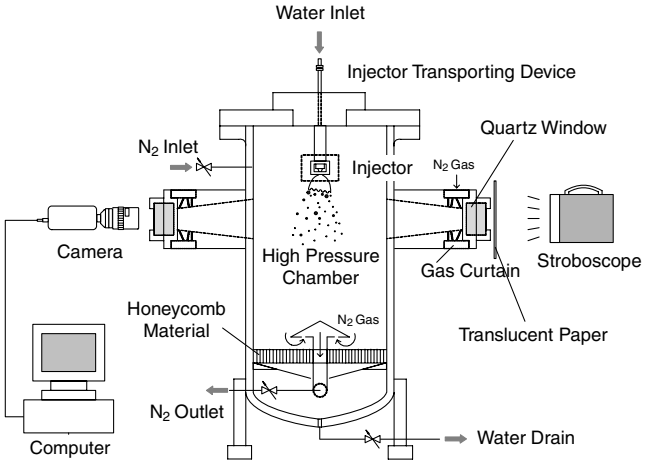

Fig. 6 Schematic diagram of high ambient pressure test for measurement of spray characteristics.

line of the orifice exit. The detected spray edge was determined using an in-house code [29]. Several criteria for breakup length have been defined in the literature; the present study defined breakup length as the continuous sheet length measured from the nozzle exit to the point where breakup occurred. To reduce breakup length uncertainties, measurements were performed at the same radial location of the spray center. To determine spray angle and breakup length, values acquired from 60 instantaneous images for each experimental case were averaged. Deviations of data were less than 10% from their mean values.

To measure the drop size of the spray, an image processing method was used [30]; the magnified images of spray drops were acquired using a high-resolution digital camera, a 180 mm macro lens (Canon EF 180 mm f/3.5 L macro-ultrasonic motor), and two 2× teleconverters (Vivitar MC 2×). The spatial resolution of each image was 2.03 μm/pixel, and 200 images were taken and averaged for each experimental case. The acquired information was postprocessed through an in-house code, as shown in Fig. 6 [30]. During the postprocessing procedures, nonspherical drops resulting from distortion or overlap were eliminated, and out-of-focus droplets were eliminated based on the gradient indicator of gray level at the droplet boundary. The detailed procedures are described in [30].

Diffraction of the lens imposed a fundamental resolution limit when a very small aperture was pursued to achieve a very small depth of field. To confirm the optical system of the present method, a calibration test was performed using a test reticle, on which four groups of circular shapes were arranged by size. The measured sizes of the circular shapes on the calibration reticle were compared with its known sizes. In the present case, the accuracy is in the order of few tens of microns, and this is confirmed by the apparent accuracy of the sizing technique for particles larger than 45 μ.

B. Numerical Setup and Calculated Conditions

The present model used KIVA-3V code to perform the computations [25]. Drop collision and coalescence were computed according to O'Rourke [31]. According to Schmidt and Rutland [32], the KIVA collision model is very sensitive to grid size and coordinator. But when a sheet is injected, the collision cannot obviously occur in the sheet itself. Therefore, the collision model applied to only product droplets [33]. The effect of the collision model was observed by the comparison of turning on/off from the viewpoint of the SMD and the spray width. The results of turning off the collision model were almost the same when compared with the results of turning on near the observation point. The original KIVA evaporation model was used for consistency of physical phenomena. In real circumstances (e.g., real propellants and very high ambient pressure over 60 bar), the original KIVA evaporation model would not be valid. A new evaporation model considering supercritical conditions or real gas effect should be adopted. But in the present study, the working fluid is water; water has a very high critical point ($Pc = 220.6$ bar and $Tc = 647$ K). The experimental conditions were a temperature of 293 K and a maximum ambient pressure of 40 bar (Table 1). Under these conditions, the quantity of vaporized droplets is negligible. Therefore, the original KIVA evaporation model rarely affects the results. To consider turbulence drop dispersion and gas turbulence modulation, the renormalization group (RNG) k-ε model [34] was used. A secondary droplet breakup model was calculated using the Taylor analogy breakup (TAB) model [25]. At the points of the primary and secondary breakups, the actual drop size was chosen from a Rosin–Rammler distribution [18]. Gas phase equations were solved using the arbitrary Lagrangian–Eulerian algorithm [25].

To reduce computing time, a two-dimensional axisymmetric grid was computed in a domain with a radius of 25 cm and a length of 100 cm, as shown in Fig. 7. This computational domain corresponded to the interior dimension of the high-pressure chamber used in the experiments. Before starting to compute, the grid dependency was checked by preliminary computations with several grid sizes (10 × 10 mm, 5 × 5 mm, 2.5 × 2.5 mm, and 1.25 × 1.25 mm). As shown in Fig. 8, the grids with 5 × 5 mm and 2.5 × 2.5 mm showed almost same SMD level. Moreover, the grids with 5 × 5 mm and 2.5 × 2.5 mm showed the same spray width. But the grid with 1.25 × 1.25 mm showed that the spray width was shifted. The reason was that the coarse grids did not capture the inner recirculation zone, even though the inner vortex existed; on the contrary, the fine grid captured the inner recirculation zone well. Actually, the calculated center of the inner recirculation zone (2.5 × 2.5 mm) existed 13 mm further upstream than the result with the 1.25 × 1.25 mm grid. Because it was not enough to check the independency of the grid, a finer grid (0.625 × 0.625 mm) was needed. As a result, the computed center of the inner recirculation zone with the finest grid showed almost the same position of the result with the 1.25 × 1.25 mm grid. The grid size, however, could not be adopted as 1.25 × 1.25 mm, because the Lagrangian–Eulerian approach's limit

Table 1 Experimental conditions and parameters

	Simulant			
	Ambient pressure, bar	Ambient gas	Pressure difference, bar	Mass flow rate, g/s
For measuring SMD	1.0	Air	3.55, 4.29, 5.79	19.99, 21.91, 25.51
For high ambient pressure	1.0, 2.0, 5.0, 10.0, 20.0, 40.0	Nitrogen	5.79	25.51

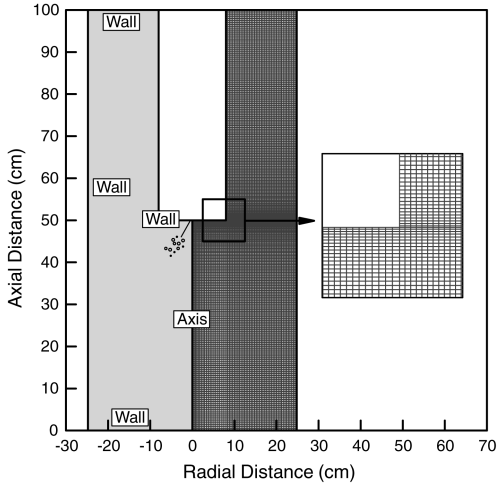

Fig. 7 Grids and boundary conditions for the computational domain.

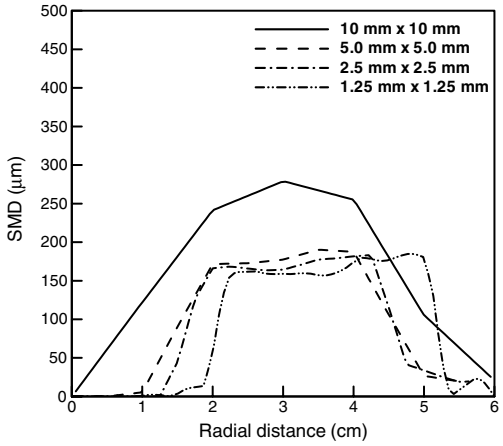

Fig. 8 SMD distributions according to various grid cell sizes.

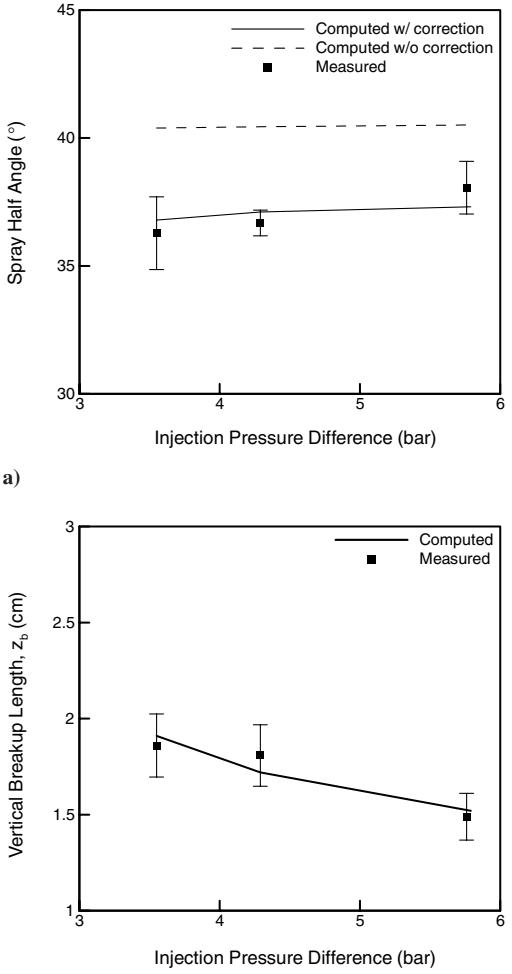

Fig. 9 Comparison of calculations with experimental results for injection pressures of 3.55, 4.29, and 5.79 bar (ambient pressure: 1 bar): a) spray half angle and b) breakup length z_b.

on the liquid mass fraction per cell should be considered. According to Karlsson [35], the liquid mass fraction, defined by the ratio liquid mass to the total mass per grid cell, should not be over 0.5. In the present calculations, the results with the 1.25×1.25 mm grid were over 0.5 near the main spray stream. Therefore, mesh spacing was nonuniform with fine resolution mesh cells in the centerline and the injector exit in order to capture the inner recirculation zone with rare spray and to predict the spray field itself well with Karlsson's [35] guide. As a result, the smallest cell was 1.8 mm wide by 1.2 mm long, which is similar to a grid size with 1.25×1.25 mm. The total number of computational cells was 13,000. The computation was set to finish at 200 ms, and initial transient results acquired in the first 10 ms were excluded in order to obtain steady-state results. Additionally, the particles impinging on the wall were excluded in the calculation, in order to reduce excessive particle stacking in a computational cell. The present model was validated by comparing the computed SMD results with the experimental results performed by Kim et al. [29]. The injection pressures were 3.55, 4.29, and 5.79 bar in an ambient pressure of 1 bar. To predict the characteristics of the spray field in high ambient pressures, the injection pressure was fixed at 5.79 bar. The detailed conditions are shown in Table 1.

IV. Results

A. Model Validations at Atmospheric Condition

The computed root spray half angle, by using the modified Eq. (3), Fig. 3, and the vertical breakup length [Eq. (31)], compared with experimental results, are as shown in Fig. 9. The computed root spray half angles [Eq. (3)] agreed closely with the measured values 5 mm downstream from the injector exit. The measured spray half angles at this location would be assumed similar to root spray angles, because it is difficult to accurately measure the spray root angles in an experiment, due to sheet deformation at the injector exit. Zong and Yang [7] pointed out that inviscid incompressible analysis overestimated the spray half angle when compared with experimental results. In the present work, the viscous effect was considered, and the predicted spray angle was corrected by Fig. 3 [9]. Also, the computed spray half angles without correction were compared with the experimental results. As shown in Fig. 9a, the results without angle correction overestimated approximately 8%; this means that it is difficult to consider all friction losses as accurately predicting spray angle. Therefore, many researchers [1,2,8] suggested empirical correlations obtained by experiments for calculating spray angle. As a result, spray half angles could be predicted accurately by such correction. The computed breakup lengths slightly overestimated the experimental results; however, deviations between computed and experimental values were within 5%. Also, decreased breakup length computed by quantitatively increasing We_2 agreed well with the experimental results. As mentioned earlier, the discharge coefficient was overpredicted, although friction loss according to the vortex chamber length was considered when the friction factor θ was over 0.25. If the discharge coefficient is overpredicted, then the injection velocity, the spray cone angle, and the breakup length are affected seriously. In the present study, the friction factor θ was near $0.15 \sim 0.17$. Therefore, the discharge coefficient was not seriously affected by friction loss due to vortex chamber length, and injection velocity, spray cone angle, and breakup length were not affected by

friction loss related to the vortex chamber length. This was another reason for accurately predicting breakup length and spray cone angle as well.

The SMD 50 mm downstream was calculated using time averaging in order to apply the same experimental method. Maximum size and main distribution width of computed SMD agreed closely with the experimental results, as shown in Fig. 10. There exists a recirculation region in the inner side of the hollow-cone spray due to the swirl of liquid, and small drops are entrained into the center of the injector. In the experiments, the measuring position was 50 mm downstream from the injector exit. In the calculation, the grid size is 2.8×3.2 mm near the measuring position. This is not an appropriate size to predict recirculation of the gas field and capture the floating drops by entrainment. This is a significant limitation of the Lagrangian–Eulerian approach and causes computed spray widths to be narrower than experimental results.

B. Model Validations at High Ambient Pressure Conditions

On the basis of the successful computational validations described previously, similar computations at higher ambient pressures (1 to 40 bar) were performed (Table 1). The computed results compared with experimental results at each ambient pressure are shown in Fig. 11. The right half of each image in Fig. 11 shows the experimental results and the left side shows the computed predictions. The computed results are vertical sectioned images to illustrate the hollow-cone structure of the spray. The agreement between experiment and computation is qualitatively good; in particular, the narrower spray widths and the shorter breakup lengths at higher ambient pressures were successfully captured by the computations. Injection pressures were the same for all cases; however, at higher ambient pressures, breakup length was shorter. According to linear stability analysis, an increased We_2 of high ambient pressure will result in a decreased breakup length, because the breakup time τ is small due to an increased Ω_s [Eqs. (25) and (26)]. A liquid sheet cannot penetrate a dense gas field and breaks into ligaments near the injector due to a decreased breakup length. The momentum of this decreased breakup length is not sufficient to drive an ambient gas field. On the contrary, the liquid field is driven by an ambient gas field. This results in a narrower spray width at higher ambient pressure. It is also difficult to observe the wavy motion of liquid sheets in experiments as the ambient pressure is increased (Fig. 11). The gas Weber number is increased as the ambient pressure is increased. Then, the breakup length is shortened dramatically by experimental observation. It is impossible to observe the wavy motion of liquid sheets because of the much shortened breakup length. To explain the reason, Eqs. (23) and (24) need to be recast in nondimensional forms. The dimensionless growth rate $\omega_r h/U$ can be expressed by the dimensionless wave number kh, We_2, viscosity, and the density ratio Q. In the long-wave region, the growth rate is dominated by $(Qkh)^{0.5}$. Also, in the short-wave region, the growth rate is dominated by $(Qk^2h^2)^{0.5}$. It indicates that the maximum growth rate of short waves increases faster than that of long waves. The faster increasing maximum growth rate shortens the breakup length abruptly [Eq. (26)].

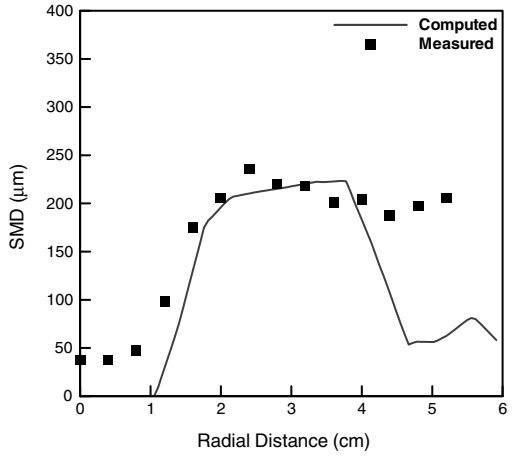

a)

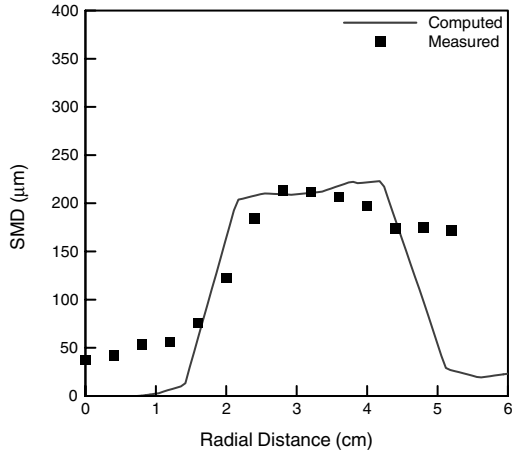

b)

Fig. 10 Comparison of SMD calculations with experimental results in an ambient pressure of 1 bar and injection pressures of a) 3.55 bar and b) 5.79 bar.

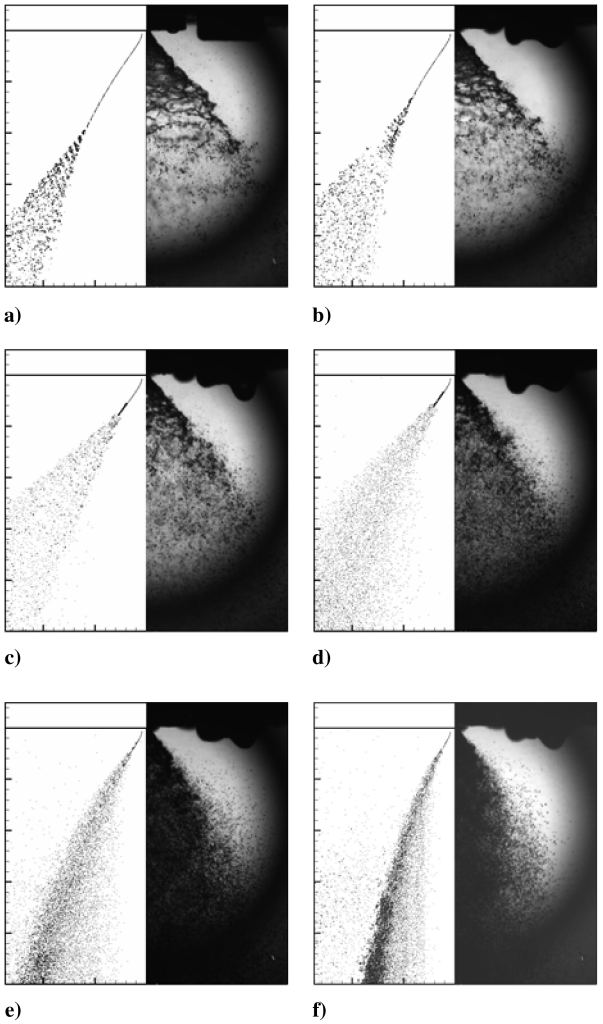

Fig. 11 Comparison of spray field calculations with experimental results with injection pressure of 5.79 bar and ambient pressures of a) 1 bar, b) 2 bar, c) 5 bar, d) 10 bar, e) 20 bar, and f) 40 bar (in each image, the left side is the computation and the right side is the experiment).

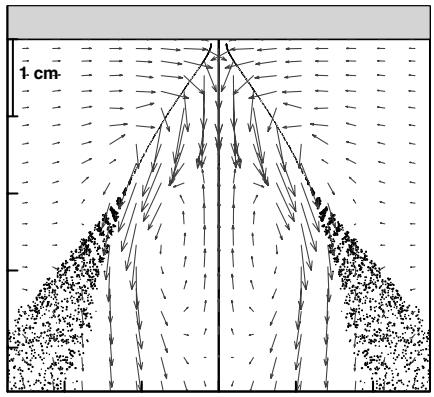

a)

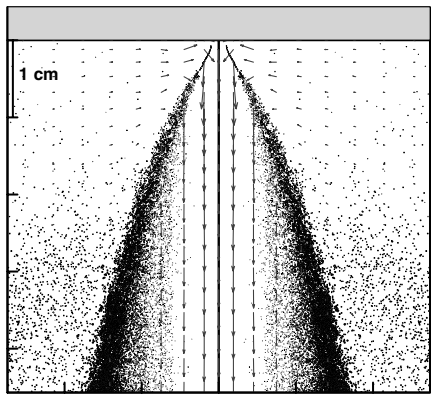

b)

Fig. 12 Inner vortex induced by injected spray with ambient pressures of a) 1 bar and b) 40 bar.

Figure 12 shows gas field vectors induced by an injected spray for ambient pressures of 1 and 40 bar. At 1 bar, the vortex driven by the sheet exists inside the spray, which appears to be related to swirl flow and the long breakup length of the liquid sheet. In the 40 bar analysis, there are swirl flows driven by the liquid sheet and very short breakup lengths. It seems that the inner vortex disappears. But an inner vortex will exist because of the swirl component of liquid flow; however, a low grid resolution cannot capture it, as shown in Fig. 12. If the inner vortex at high ambient pressure could be captured, grids with high resolution must be used to calculate the spray field; however, this is more expensive. Also, the Lagrangian–Eulerian approach has a limitation, such that a fine grid is not applicable due to droplet size, as described earlier [35]. Additional research is needed to efficiently capture the inner vortex at high ambient pressure.

Predicted breakup lengths and local spray half angles at high ambient pressures are compared with experimental results in Fig. 13. The predicted breakup lengths were obtained the same way as described in the experimental setup. When We_2 ($P_{\text{amb}} = 1$ bar) is approximately 0.84, the computed breakup lengths agreed well with the measured results. However, at higher We_2 values, the computed values underestimated the breakup lengths when compared with the measured lengths. According to Davy and Loustalan [12], sheet breakup occurs within a few millimeters of the nozzle exit: a region of the spray that is too dense to allow the use of conventional laser-based measurement techniques. Moreover, the use of conventional photographic lighting techniques may produce misleading results in this region of the spray. Therefore, it is difficult to distinguish a sheet region from a dense spray field at a high ambient pressure. Hence, the measured breakup length values may include both sheet and ligament regions. Figure 13a shows that computed breakup lengths, which included a ligament region, agreed with experimental results when compared with the computed breakup length, excluding a ligament region. Figure 13b shows the comparison of predicted and experimental values of the spray half angle at 10 mm downstream from the

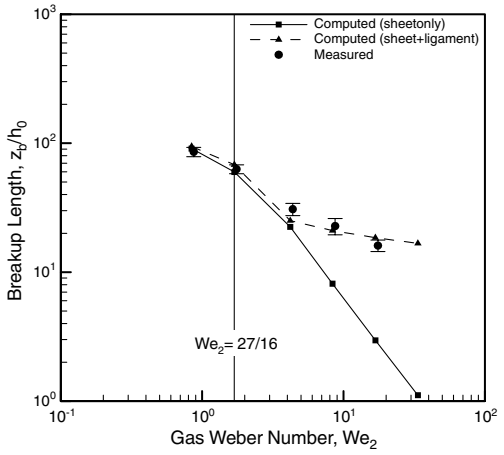

a)

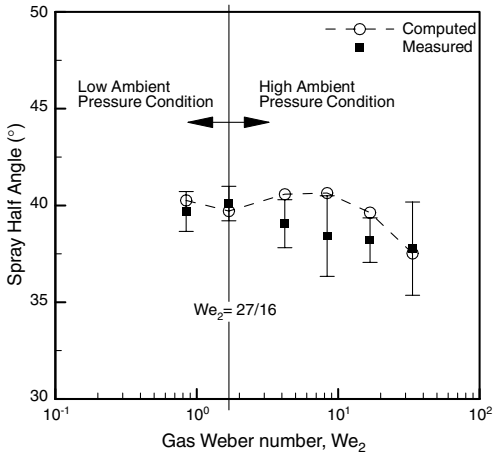

b)

Fig. 13 Comparisons of the computed results with experimental results according to increase of We_2: a) dimensionless breakup length and b) spray half angle at 10 mm downstream from injector exit.

injector exit. To define the computed local spray half angle, the liquid mass fraction per *i*th cell volume

$$f_{i,\text{liq}} = \left[\sum_n \rho_{liq} N_n \frac{\pi}{6} D_n^3 \Big/ \left(\rho_{\text{gas}} \delta V + \sum_n \rho_{\text{liq}} N_n \frac{\pi}{6} D_n^3\right)\right]_i$$

was used. First, at the axial location 10 mm downstream from the injector exit, the distribution of liquid mass fraction was checked. Then, the spray angle at 80% of the maximum value was calculated. In reality, it was observed that the gradient of the liquid mass fraction was decreased abruptly in the region $f_{i,\text{liq}} < 0.8 < f_{i,\max}$. Therefore, the criterion of the spray angle was determined as 80% of the maximum liquid mass fraction at the axial location 10 mm downstream from the injector exit. In all cases, the initial spray half angle was 37.14 deg, because the same injector pressure differences were used. However, as the spray progresses downstream, the spray angle decreased, because the spray curved inside due to ambient gas flow effects on the spray field [29]. Furthermore, under high ambient pressures, downstream spray angles became narrower due to fast atomization related to short breakup lengths (Fig. 11). These observations agreed with those of Kim et al. [29]. But, as shown in Fig. 13b, the local spray half angles were overpredicted in ambient pressure over 5 bar but still within measurement deviation. At ambient pressures 1 and 2 bar, the liquid sheet existed at 10 mm downstream, as shown in Fig. 13a. But, if ambient pressure was over 5 bar, the sheet broke into ligament, and the ligament broke into droplets very quickly. Schmidt et al. [36] performed numerical

simulation on pressure-swirl atomizers, and they reported that the same results were experienced. They indicated several reasons for overprediction of spray cone angle: the experimental error, less numerical dispersion than experimental data, and an underestimate of turbulent drop dispersion. As mentioned previously, the spray cone angles agreed well with the experimental data at ambient pressures of 1 and 2 bar; that is, the prediction of the liquid sheet spray cone angle was valid. For the secondary breakup of droplets, the TAB model was used. According to Papageorgakis and Assanis [37], due to the empirical nature of the TAB model, predicted spray behavior has often not been in satisfactory agreement with experimental results. However, the differences were small (within 5%) when compared with the experimental results. At 10 mm downstream from the injector exit, the spray field was not affected seriously by the ambient gas field [29]. In this study, there were no large differences between the measured and the predicted initial values. The computed and measured angles were quantitatively similar within the measurement deviations.

In high ambient pressures, SMD was predicted 50 mm downstream from the injector exit, as shown in Fig. 14. Figure 14a shows that at high ambient pressures lower than 5 bar, the predicted SMD is smaller. On the contrary, SMD was larger at ambient pressures higher than 5 bar. At high ambient pressures, fast atomization can result in the generation of small drops near the injector exit. Senecal et al. [13] pointed out that secondary drop breakup was found to be important in high ambient pressure case. Also, they reported that the effect of increased ambient pressure and density was very significant: the short breakup length and small droplets were due to the high growth rate, and Eq. (24) indicated that high density ratios created faster wave growth [12]. In the results of this study, a similar qualitative trend could be observed experimentally and computationally. As shown in Fig. 11, the experimental downstream spray fields at an ambient pressure of 10 bar or higher were too dense to be penetrated by a light source. That's the reason why Kim et al. [29] could not obtain SMD data under high ambient pressure. Because the measured SMD was absent, the predicted SMD was not validated, but the decreased breakup length was consistent with the experimental results. Such dense spray can increase collision and coalescence activities between droplets. Figure 14b shows the computed SMD according to the axial position in an ambient pressure of 40 bar, and it shows that SMD increases as the axial measuring position moves further from the injector exit. This suggests that the collision and coalescence processes are more dominant than the breakup process at high ambient pressures. In our high ambient pressure experiments, it was difficult to measure SMD precisely by using the photographic techniques adopted by this study, because the spray was too dense, as mentioned earlier. At an ambient pressure of 40 bar, it was impossible to recognize droplets in the dense spray field in experiments. But as Schmidt and Rutland [32] pointed out, the original KIVA collision model is very sensitive to grid size. As mentioned earlier, although the grid independency was fulfilled, a more accurate collision model is needed. To minimize the uncertainties related to collision in the results from experiments and computations, a new technique for measuring SMD in high pressures should be developed. To investigate the collision process numerically, a new model (like the recent collision process models [38,39]) should be considered for such computations.

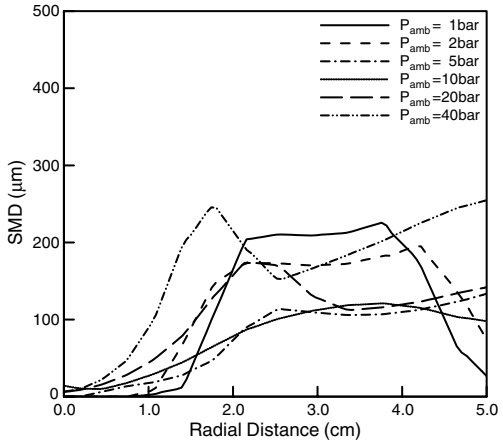

a)

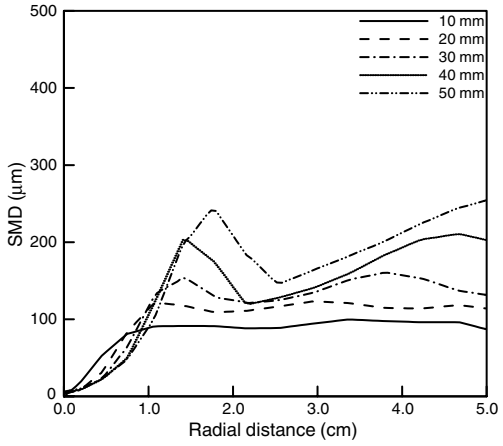

b)

Fig. 14 Predictions of SMD distribution: a) along radial distance at 50 mm downstream for each ambient pressure condition, and b) according to axial position from injector exit at an ambient pressure of 40 bar.

V. Conclusions

A sheet breakup model using linear stability theory was improved by liquid viscous theory for obtaining the initial liquid sheet properties as spray inlet conditions. The initial characteristics of the liquid sheet, including film thickness, spray cone angle, and injection velocity, were predicted by using swirl injector design procedures, considering pressure losses due to friction. At low gas Weber numbers (i.e., low ambient gas pressures), the sheet broke up as long waves. At high ambient gas pressures, Weber numbers are higher due to high gas density, although the initial characteristics of the swirl injector have not changed. Using these observations, simplified dispersion relations for the two breakup regimes were applied to predict characteristics of a swirl injector installed in a LPRE.

To validate the sheet breakup model, a single swirl injector with various pressure differences was tested at various ambient pressure conditions. For the SMD comparison of predicted values with experimental results, two different injection pressures performed at atmospheric conditions were adopted. Agreement between the predicted and experimental results was good for SMD, breakup length, and spray distribution.

To compare the predicted characteristics of spray in high-pressure conditions, the injector (with the same injection velocity) was tested as the ambient pressure increased. As gas Weber numbers increased, the predicted breakup lengths were shortened. These predictions agreed closely with experimental results, both qualitatively and quantitatively. Throughout these high ambient pressure comparisons, the measured breakup lengths included both ligaments and sheets, because it was difficult for photographic techniques to recognize the breakup length precisely in our high-ambient-pressure experiments.

Although the six different gas Weber numbers had the same liquid Weber number, the spray cone angle changed due to ambient gas flow. This phenomenon was observed, qualitatively and quantitatively, in both predicted and experimental results. The prediction of SMD indicated that, as ambient pressure increased, the predicted SMD decreased at 50 mm downstream of the injector exit. However, at high ambient pressures, the predicted SMD increased. In this experimental condition, collision and coalescence were more common than breakup. This observation should be validated using a

detailed collision model, and further collision experiments at high ambient pressures should be performed.

Appendix

Dityakin et al. [9] considered hydraulic loss related to the swirling chamber length. To find the hydraulic loss, a liquid element volume with the element length dL was adopted. A liquid element volume is defined by $dV = \pi(r_k^2 - r_r^2)dL$. The frictional force acting on the external surface of this element can be expressed as

$$dF = \frac{\lambda_\sigma}{4}\frac{\rho V^2}{2}2\pi r_k dL \tag{A1}$$

Here, λ_σ is a friction coefficient and V is a liquid velocity. Energy loss for the liquid element volume can be presented in the form:

$$dE = \frac{\lambda_\sigma}{4}\frac{2r_k}{r_k^2 - r_r^2}\frac{\rho V^2}{2}ds \tag{A2}$$

Here, ds is a length of liquid element path. Then, Eq. (11) will be obtained by integrating Eq. (A2) with assumption 1) an axial velocity is assumed constant; therefore, a tangential velocity is affected by the frictional force; and assumption 2) $r_k + r_r \approx 2r_k$ because of small film thickness. More details are represented in [1,8–10].

Acknowledgments

This research was supported by the Korea Aerospace Research Institute (Korea Space Launch Vehicle program). This research was also supported by the National Research Foundation of Korea Grant (2009-0053283) and the National Space Lab Program (S10801000194-08A0100-19410) through the National Research Foundation of Korea, funded in part by the Ministry of Education, Science, and Technology and the Institute of Advanced Aerospace Technology.

References

[1] Bayvel, L., and Orzechowski, Z., *Liquid Atomization*, Taylor and Francis, Washington, DC, 1993.

[2] Lefebvre, A. H., *Atomization and Sprays*, Hemisphere, New York, 1989.

[3] Rubinsky, V. R., "Combustion Instability in the RD-0110 Engine," *Liquid Rocket Engine Combustion Instability*, edited by V. Yang, and W. E. Anderson, Progress in Astronautics and Aeronautics, AIAA, Washington, DC, 1995, pp. 89–112.

[4] Sutton, G. P., *History of Liquid Propellant Rocket Engines*, AIAA, Reston, VA, 2006.

[5] Sutton, G. P., "History of Liquid-Propellant Rocket Engines in Russia, Formerly the Soviet Union," *Journal of Propulsion and Power*, Vol. 19, No. 6, 2003, pp. 1008–1037. doi:10.2514/2.6943

[6] Rizk, N. K., and Lefebvre, A. H., "Influence of Liquid Film Thickness on Airblast Atomization," *Journal of Engineering for Power*, Vol. 102, No. 3, 1980, pp. 706–710. doi:10.1115/1.3230329

[7] Zong, N., and Yang, V., "Cryogenic Fluid Jets and Mixing Layers in Transcritical and Supercritical Environments," *Combustion Science and Technology*, Vol. 178, Nos. 1–3, 2006, pp. 193–227. doi:10.1080/00102200500287613

[8] Borodin, V. A., Dityakin, Y. F., Klyachko, L. A., and Tgodkin, V. L., "Atomization of Liquids," Air Force Foreign Technology Div. Rept. FTP-MT-24-97-68 (AD685151), Dayton, OH, 1968.

[9] Dityakin, Yu. F., Klyachko, L. A., Novikov, B. V., and Yagodkin, V. I., "*Liquid Atomization*," Mashinostroenie, Moscow, 1977 (in Russian).

[10] Bazarov, V. G., Yang, V., and Puri, P., "Design and Dynamics of Jet and Swirl Injectors," *Liquid Rocket Thrust Chambers: Aspects of Modeling, Analysis, and Design*, edited by V. Yang, M. Habiballah, J. Hulka, and M. Popp, Progress in Astronautics and Aeronautics, AIAA, Reston, VA, Vol. 200, 2004, pp. 19–103.

[11] Inamura, T., Tamura, H., and Sakamoto, H., "Characteristics of Liquid Film and Spray Injected from Swirl Coaxial Injector," *Journal of Propulsion and Power*, Vol. 19, No. 4, 2003, pp. 632–639. doi:10.2514/2.6151

[12] Davy, M. H., and Loustalan, P. W., "On the Sheet Breakup of Direct-Injection Gasoline Pressure-Swirl Atomizer Sprays," *Atomization and Sprays*, Vol. 17, No. 6, 2007, pp. 501–528. doi:10.1615/AtomizSpr.v17.i6.20

[13] Senecal, P. K., Schmidt, D. P., Nouar, I., Rutland, C. J., Reitz, R. D., and Corradini, M. L., "Modeling High-Speed Viscous Liquid Sheet Atomization," *International Journal of Multiphase Flow*, Vol. 25, Nos. 6–7, 1999, pp. 1073–1097. doi:10.1016/S0301-9322(99)00057-9

[14] Dombrowski, N., and Johns, W. R., "The Aerodynamic Instability and Disintegration of Viscous Liquid Sheets," *Chemical Engineering Science*, Vol. 18, No. 3, 1963, pp. 203–214. doi:10.1016/0009-2509(63)85005-8

[15] Stapper, B. E., Sowa, W. A., and Samuelson, G. S., "An Experimental Study of the Effects of Liquid Properties on the Breakup of a Two-Dimensional Liquid Sheet," *Journal of Engineering for Gas Turbines and Power*, Vol. 114, No. 1, 1992, pp. 39–45. doi:10.1115/1.2906305

[16] Dombrowski, N., and Hassan, D., "The Flow Characteristics of Swirl Centrifugal Spray Pressure Nozzles with Low Viscosity Liquids," *AIChE Journal*, Vol. 15, No. 4, 1969, pp. 604–611. doi:10.1002/aic.690150424

[17] Jones, A. R., "Design Optimization of a Large Pressure-Jet Atomizer for Power Plant," *Proceedings of the 2nd International Conference on Liquid Atomization and Spray Systems*, ICLASS, Madison, WI, 1982, pp. 181–185.

[18] Han, Z., Parrish, S., Farrell, P. V., and Reitz, R. D., "Modeling Atomization Processes of Pressure-Swirl Hollow-Cone Fuel Sprays," *Atomization and Sprays*, Vol. 7, No. 6, 1997, pp. 663–684.

[19] Ren, W. M., and Nally, J. F., "Computations of Hollow-Cone Sprays from a Pressure-Swirl Injector," Society of Automotive Engineers Paper 982610, 1998.

[20] Binnie, A. M., and Harris, D. P., "The Application of Boundary Layer Theory to Swirling Liquid Flow Through a Nozzle," *Quarterly Journal of Mechanics and Applied Mathematics*, Vol. 3, No. 1, 1950, pp. 80–106. doi:10.1093/qjmam/3.1.80

[21] Sterling, A. M., and Sleicher, C. A., "The Instability of Capillary Jets," *Journal of Fluid Mechanics*, Vol. 68, No. 3, 1975, pp. 477–495. doi:10.1017/S0022112075001772

[22] Reitz, R. D., and Bracco, F. V., "Mechanisms of Breakup of Round Liquid Jets," *Encyclopedia of Fluid Mechanics*, Gulf Publishing, Houston, TX, 1986, pp. 233–249.

[23] Li, X., and Tankin, R. S., "On the Temporal Instability of a Two-Dimensional Viscous Liquid Sheet," *Journal of Fluid Mechanics*, Vol. 226, May 1991, pp. 425–443. doi:10.1017/S0022112091002458

[24] Lin, S. P., "Two Types of Linear Theories for Atomizing Liquids," *Atomization and Sprays*, Vol. 16, No. 2, 2006, pp. 147–158. doi:10.1615/AtomizSpr.v16.i2.20

[25] Amsden, A. A., "KIVA-3V: A KIVA Program with Block-Structured Mesh for Complex Geometries," Los Alamos National Lab., TR LA-12503-MS, Los Alamos, NM, 1993.

[26] Zong, N., "Modeling and Simulation of Cryogenic Fluid Injection and Mixing Dynamics under Supercritical Conditions," Ph.D. Dissertation, Pennsylvania State Univ., University Park, PA, 2005.

[27] Sirignano, W. A., and Mehring, C., "Review of Theory of Distortion and Disintegration of Liquid Streams," *Progress in Energy and Combustion Science*, Vol. 26, No. 4–6, 2000, pp. 609–655. doi:10.1016/S0360-1285(00)00014-9

[28] Dombrowski, N., and Hooper, P. C., "The Effect of Ambient Density on Drop Formation in Sprays," *Chemical Engineering Science*, Vol. 17, No. 4, 1962, pp. 291–305. doi:10.1016/0009-2509(62)85008-8

[29] Kim, D., Im, J-H., Koh, H., and Yoon, Y., "Effect of Ambient Gas Density on Spray Characteristics of Swirling Liquid Sheets," *Journal of Propulsion and Power*, Vol. 23, No. 3, 2007, pp. 603–611. doi:10.2514/1.20161

[30] Kim, D., Kim, S., Han, P., and Yoon, Y., "Effect of Recess on Mixing and Atomization Characteristics of Liquid–Liquid Swirl Coaxial Injectors," *Atomization and Sprays* (in press).

[31] O'Rourke, P. J., "Collective Drop Effects on Vaporizing Liquid Sprays," Ph.D. Dissertation, Princeton Univ., 1981.

[32] Schmidt, D. P., and Rutland, C. J., "Reducing Grid Dependency in Droplet Collision Modeling," *Journal of Engineering for Gas Turbines and Power*, Vol. 126, No. 2, 2004, pp. 227–233. doi:10.1115/1.1564066

[33] Reitz, R. D., "Modeling Atomization Processes in High-Pressure Vaporizing Sprays," *Atomisation and Spray Technology*, Vol. 3, No. 4,

1987, pp. 309–337.
[34] Han, Z., and Reitz, R. D., "Turbulence Modeling of Internal Combustion Engines Using RNG k-ε Models," *Combustion Science and Technology*, Vol. 106, Nos. 4–6, 1995, pp. 267–295. doi:10.1080/00102209508907782
[35] Karlsson, J. A. J., "Modeling Auto-Ignition, Flame Propagation and Combustion in Non-Stationary Turbulent Sprays," Ph.D. Dissertation, Chalmers Univ. of Technology, Göteborg, Sweden, 1995.
[36] Schmidt, D. P., Nouar, I., Senecal, P. K., Rutland, C. J., Martin, J. K., Reitz, R. D., and Hoffman, J. A., "Pressure-Swirl Atomization in the Near Field," Society of Automotive Engineers Paper 1999-01-0496, 1999.
[37] Papageorgakis, G. C., and Assanis, D. N., "A Spray Breakup Model for Low Injection Pressures," *International Communications in Heat and Mass Transfer*, Vol. 23, No. 1, 1996, pp. 1–10. doi:10.1016/0735-1933(95)00079-8
[38] Munnannur, A., and Reitz, R. D., "A New Predictive Model for Fragmenting and Non-Fragmenting Binary Droplet Collisions," *International Journal of Multiphase Flow*, Vol. 33, No. 8, 2007, pp. 873–896. doi:10.1016/j.ijmultiphaseflow.2007.03.003
[39] Post, S. L., and Abraham, J., "Modeling the Outcome of Drop-Drop Collisions in Diesel Sprays," *International Journal of Multiphase Flow*, Vol. 28, No. 6, 2002, pp. 997–1019. doi:10.1016/S0301-9322(02)00007-1

D. Talley
Editor-in-Chief